atmospheric subsidence associated with the Walker circulation, or the atmospheric large-scale zonal circulation. May 1998 corresponded to the transition period in terms of the Walker circulation: just after the large-scale subsidence over the western Pacific was relaxed, and just before the subsidence over the eastern Pacific was established. We consider that the relatively warm homogeneous SST distribution, without suppression of convection by large-scale subsidence, allowed the unusual global propagation of the MJO precipitation.

Another notable feature of this MJO was that it influenced the termination of the El Niño through the intensification of the easterly trade winds. A triggering effect of westerly wind bursts (associated with the MJO) on the initiation of El Niño events has been previously suggested[3–8]. However, there have been no previous observations of the MJO that triggered the termination of El Niño events.

How an MJO influences the ocean depends on its dynamical structure. The MJO is usually considered to have the Rossby wave response of the 'Matsuno-Gill pattern' to the west of the convection centre. The intensification of the twin vortices from the Rossby wave response is favourable for the occurrence of westerly wind bursts. In our case, however, the lower-tropospheric disturbance lacked the Rossby wave response and had only the Kelvin wave response.

Wang and Xie[17] studied theoretically the effects of mean wind shear on atmospheric equatorial waves. Their results indicated that the westerly wind shear (stronger westerly wind upward) traps the Rossby waves in the upper troposphere, while not much affecting the Kelvin waves. In our case, the mean zonal-wind difference between the 200-hPa and 850-hPa levels was 6.9 $m\,s^{-1}$, which is comparable to the 10 $m\,s^{-1}$ that Wang and Xie assumed[17].

Thus, the mean wind field not only allowed the global propagation of a convectively coupled MJO, but also affected its structure, suppressing the Rossby wave response in the lower troposphere. The resultant lower-tropospheric Kelvin wave disturbance superposed on the mean easterly winds in turn caused the intensification of the easterly trade winds, and brought about an unusual easterly-wind effect of the MJO on El Niño.

Slingo *et al.*[18] suggested an important link between the MJO and the basic climate by comparing the performances of general circulation models. The May 1998 event re-emphasizes the significance of multi-scale interactions within the climate system, on which further studies are required. □

Received 4 June; accepted 20 September 1999.

1. Madden, R. A. & Julian, P. R. Detection of a 40–50 day oscillation in the zonal wind in the tropical Pacific. *J. Atmos. Sci.* **28,** 702–708 (1971).
2. Madden, R. A. & Julian, P. R. Description of global scale circulation cells in the tropics with a 40–50 day period. *J. Atmos. Sci.* **29,** 1109–1120 (1972).
3. McPhaden, M. J. Genesis and evolution of the 1997–98 El Nino. *Science* **283,** 950–954 (1999).
4. Nitta, Ts. & Motoki, T. Abrupt enhancement of convective activity and low level westerly wind burst during the onset phase of 1986–87 El Nino. *J. Meteorol. Soc. Jpn* **65,** 497–506 (1987).
5. Nitta, Ts. Development of a twin cyclone and westerly wind bursts during the initial phase of 1986–87 El Nino. *J. Meteorol. Soc. Jpn* **67,** 677–681 (1989).
6. Nitta, Ts., Mizuno, T. & Takahashi, K. Multi-scale convective systems during the initial phase of 1986/87 El Nino. *J. Meterol. Soc. Jpn* **70,** 317–335 (1992).
7. Kindle, J. C. & Phoebus, P. A. The ocean response to operational westerly wind bursts. *J. Geophys. Res.* **100,** 4893–4920 (1995).
8. Lau, K. M. & Chan, P. H. The 40–50 day oscillation and the El Niño/Southern Oscillation: A new perspective. *Bull. Am. Meteorol. Soc.* **67,** 533–534 (1986).
9. Suarez, M. J. & Schopf, P. S. A delayed action oscillator for ENSO. *J. Atmos. Sci.* **45,** 3283–3287 (1988).
10. Battisti, D. S. Dynamics and thermodynamics of a warming event in a coupled tropical atmosphere-ocean model. *J. Atmos. Sci.* **45,** 2889–2919 (1988).
11. Wentz, F. J. & Spencer, R. W. SSM/I rain retrievals within a unified all-weather ocean algorithm. *J. Atmos. Sci.* **55,** 1613–1627 (1998).
12. Shibata, A., Imaoka, K., Kachi, M. & Murakami, H. SST observation by TRMM Microwave Imager aboard Tropical Rainfall Measuring Mission. *Umi no Kenkyu* **8,** 135–139 (1999). (In Japanese.)
13. Harrison, D. E. & Vecchi, G. A. On the termination of El Niño. *Geophys. Res. Lett.* **26,** 1593–1596 (1999).
14. Matsuno, T. Quasi-geostrophic motions in the equatorial area. *J. Meteorol. Soc. Jpn* **44,** 25–43 (1966).
15. Gill, A. E. Some simple solutions for heat-induced tropical circulation. *Q. J. R. Meteorol. Soc.* **106,** 447–462 (1980).
16. Wang, B. & Rui, H. Synoptic climatology of transient tropical intraseasonal convection anomalies: 1975–1985 *Meteorol. Atmos. Phys.* **44,** 43–61 (1990).
17. Wang, B. & Xie, X. Low-frequency equatorial waves in vertically sheared zonal flow. Part I: Stable waves. *J. Atmos. Sci.* **53,** 449–467 (1996).
18. Slingo, J. M. *et al.* Intraseasonal oscillations in 15 atmospheric general circulation models: results from an AMIP diagnostic subproject. *Clim. Dyn.* **12,** 325–357 (1996).

Acknowledgements

We thank T. Nakazawa, Y. Suzuki, H. Fujinami, K. Imaoka and H. Murakami for help with processing the SSM/I and TRMM data.

Correspondence and requests for materials should be addressed to Y.N.T.

Combined dynamic and geochemical evidence for convergent melt flow beneath the East Pacific Rise

Marc Spiegelman* & Jennifer R. Reynolds*†

* *Lamont-Doherty Earth Observatory, Palisades, New York 10964, USA*

Determining the flow of magma and solid mantle beneath mid-ocean ridges is crucial for understanding the dynamics of plate spreading and the formation of new oceanic crust. Theoretical models suggest a range of possible flow regimes—from passive, plate-driven flows[1,2] to 'active', buoyantly driven solid convection[3–7]—and have spurred an ambitious field programme to attempt to distinguish these flow fields using geophysical techniques[8]. Models that explore the geochemical consequences of melt transport[9], however, suggest that these different flow fields can also have distinctive geochemical signatures. Here we compare model predictions to the chemistry of well located and closely sampled basalts from across the ridge-crest of the fast-spreading East Pacific Rise at 12° N (refs 10–12). These data show features that are not explained by traditional geochemical models of ocean-ridge magma generation, yet are consistent with the geochemical consequences of the new transport models that have passive mantle flow and convergent lateral melt migration. These results are also consistent with those of the seismic MELT experiment[8], but add new information about the relative flow of melt and solid in the mantle which is probably unmeasurable by geophysical techniques.

The melt and solid flow fields for two end-member flow regimes proposed for mid-ocean ridges are shown in Fig. 1 (see ref. 9 for detailed discussion). In the regime shown in Fig. 1a, the solid mantle flow is driven by the spreading plates, producing a broad region of upwelling and melting (passive flow). The melt flow, however, is focused towards the ridge axis by pressure gradients induced by viscous stresses[1,2]. In Fig. 1b, the solid mantle flow is driven both by the plates and by buoyancy forces induced by lateral variations in melt content (active flow). The buoyancy forces become significant at lower mantle viscosities, and drive small-scale mantle convection that promotes more rapid upwelling within a narrow region beneath the ridge axis[3–7]. The lower viscous stresses, however, eliminate any significant convergent melt flow.

The outstanding question has been how to distinguish between these theoretical models using geological and/or geophysical observations. Both calculations in Fig. 1 form similar crustal thicknesses within a relatively narrow crustal accretion zone. Both calculations have the same maximum degree of melting and permeability functions, and produce mantle porosities that would probably be

† Present address: Monterey Bay Aquarium Research Institute, PO Box 628, 7700 Sandholt Rd, Moss Landing, California 95039, USA.

difficult to distinguish using physical techniques. Nevertheless, these flow calculations have distinct geochemical signatures which suggest that compositional variations in erupted magmas may be sensitive indicators of mantle dynamics[9].

Figure 2 illustrates the geochemical signatures of these calculations for the simplest problem of trace elements with constant bulk partition coefficients and a uniform source composition. The flow models predict variations in both overall melt composition and in the spatial distribution of erupted compositions which can be significantly different from those calculated using models that neglect melt transport (see, for example, refs 13, 14). These variations are a direct consequence of the ability of melt and solid to travel, and mix, on different trajectories in two and three dimensions[9]. Convergent melt flow relative to solid flow (Fig. 1a) enriches the concentration of incompatible trace elements at the ridge axis by adding lower-degree melts from a wide region. Convergent solid flow within the partially molten region (Fig. 1b), however, produces axial melts that are extremely depleted in the most incompatible elements. These elements are removed by small amounts of melting and transport that occur off-axis before the solid undergoes most of its melting within the narrow upwelling zone. These two models also predict completely opposite signatures in the relative enrichment of incompatible trace elements in on-axis and off-axis melts (Fig. 2). The passive flow model produces magmas that are most enriched on-axis but become more depleted with distance off-axis within the crustal accretion zone (~5 km half-width in Fig. 1a). This result is an unusual consequence of convergent melt flow in open systems. In contrast, the active flow model produces melts that become more enriched with distance off-axis, as do melting models that neglect transport.

The spatial trend of incompatible trace element enrichment or depletion is a robust consequence of the relative geometries of the melt and solid flow fields, and depends only on whether melt or solid flow is convergent. For this reason, we concentrate on comparing the composition of well located on- and off-axis lavas with similar sources. We also consider more quantitative details such as the amplitude of the signals and the width of the crustal accretion zone; however, these are more dependent on specific model parameters, and will be explored in depth elsewhere.

A detailed petrological and geological study around 12° N on the East Pacific Rise[10–12] provides important data and interpretation that can be compared to predictions from the theoretical flow models. The study area (Fig. 3) covers 50 km of ridge axis, and extends 8 km west and 10 km east of the axis. Basaltic glasses from 143 rock core and dredge samples have been analysed by electron microprobe, and 52 samples (Fig. 3c) have also been analysed for major and trace elements by direct-current plasma spectrometry (DCP). Samples with full analyses form a 'training set' for classifying the remaining samples using a nearest-neighbour algorithm. Geological information is drawn from multi-beam bathymetry[15], SeaMARC I side-scan sonar[16] and camera tows. Further details are given elsewhere[12].

Within the "axial summit trough"[17], one finds both normal mid-ocean-ridge basalts (N-MORBs) and small-volume eruptions of incompatible-trace-element enriched MORBs (T-MORBs) (Fig. 3), with remarkably few samples showing compositional evidence of simple mixing despite evidence for an axial magma chamber in this area[18]. These observations suggest that, at 12° N, individual melts

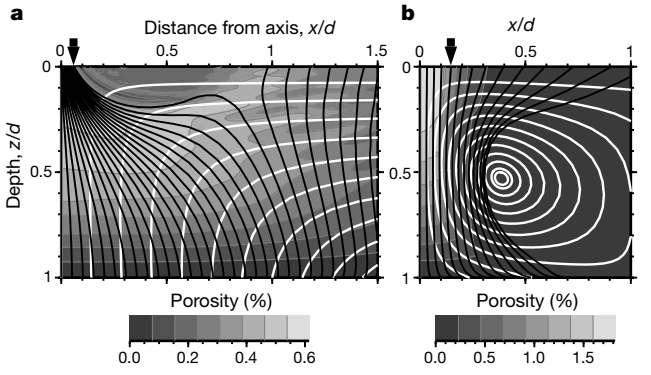

Figure 1 Two-dimensional calculations of melt and solid mantle flow beneath mid-ocean ridges for two end-member flow regimes. The diagrams are vertical cross-sections of the right half of the melting region. Horizontal (x) and vertical (z) distances are scaled to the depth where melting begins ($d \approx 80$–100 km). The black curves represent melt flow, while white curves represent solid mantle flow. The melting rate is proportional to the solid upwelling rate, and no melting occurs in downwelling regions or previously melted mantle. Both solutions have linear melting functions with maximum degree of melting $F_{max} \approx 20\%$ and the same permeability function[9]. Arrows mark the width of the ''crustal accretion region'', defined as the zone over which ~85% of the melt produced within the box is added to the crust. If the crustal thickness produced over this region is h, then the depth scale is set by $d = h/0.075$ (that is, 6 km of crust implies $d = 80$ km). **a**, Passive, plate-driven flow. When solid mantle flow is dominated by plate motion, large pressure gradients due to shear in the viscous matrix can focus the flow of melt towards the spreading centre. **b**, 'Active' buoyancy driven flow. At lower mantle viscosities or slower plate velocities, variations in melt content drive more rapid upwelling beneath the spreading centre. The width of the upwelling and melting region narrows in compensation.

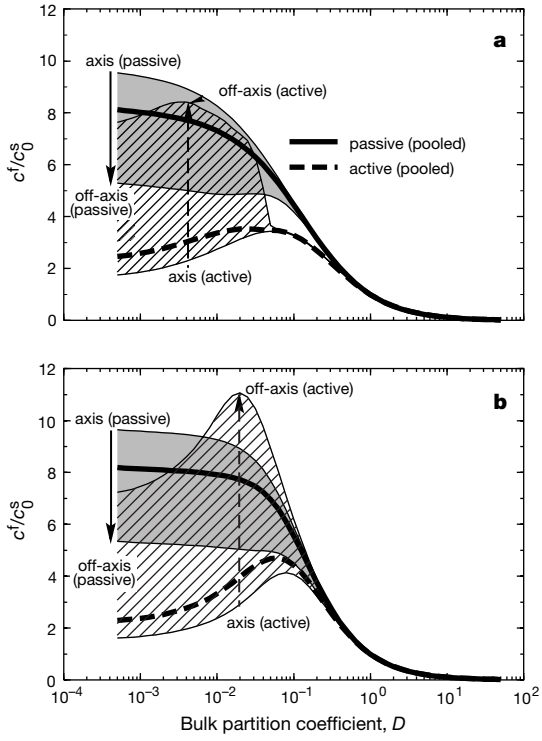

Figure 2 The geochemical signatures of the two flow models shown in Fig. 1. Results are shown for two end-member equilibration models of equilibrium transport (**a**) and disequilibrium transport (**b**), which are the open-system analogues of batch and fractional melting[9]. Each panel shows the range of melt compositions produced by the different models for trace elements with constant bulk partition coefficients. All melt concentrations (c^f) are normalized to the unmelted solid source (c_0^s). The shaded fields show results for the passive flow model, the hatched fields for the active model. The thin lines bounding these fields show the range of concentration patterns for melts 'erupted' between the axis ($x = 0$) and the off-axis edge of the accretion zone marked by arrows in Fig. 1 ($x = 0.06d$ for passive flow; $x = 0.14d$ for active flow). Heavy lines show the mean concentrations in the accretion zone, calculated as the sum of all the local melts weighted by their flux[9]. **a**, Equilibrium transport where melt and solid continuously re-equilibrate during transport. **b**, Disequilibrium transport which assumes fractional melting of the solid with mixing of incremental melts occurring along melt flow lines.

can preserve chemical differences through the crustal accretion process. In addition, Reynolds and Langmuir[12] have also identified a petrologically distinct lava type that only erupts off-axis (red symbols in Fig. 3a). In their original 1992 paper[10], samples of this lava type were considered part of the temporal variation at the 12° N axis, and contributed scatter. When these samples are removed, the temporal variation in axial larva composition is even more systematic. The off-axis magma type is most readily identified in depleted compositions. Because of this, and to minimize the complicating effect of mantle source variations, we limit discussion here to N-MORB compositions and refer to the off-axis type as OA-N-MORB. The contrast between this lava type and the N-MORBs erupted on-axis form the basis for testing model predictions of melt and solid mantle flow.

Many samples of the OA-N-MORB type can clearly be identified with morphological features suggestive of off-axis eruption[11,12] such as small seamounts (Fig. 3a), or flows and pillow mounds that cover abyssal hill faults (Fig. 3b). Observations during dives of the *Alvin* submersible at 9° 31′ N and 9° 50′ N have also documented small off-axis lava flows and volcanic constructions in that region[17,19,20]. Of the 20 OA-N-MORB samples found at 12° N, 45% can be positively associated with features indicating off-axis eruption despite the incomplete side-scan coverage and limitations of mapping resolution. No sample of this composition type is found on the EPR axis here. A search of 123 earlier dredges along the EPR from 5° to 14° N identified seven OA-N-MORB samples off-axis elsewhere[12]. No such samples were found along the axis, with a single exception from the intersection with the Clipperton transform.

For the samples with full major- and trace-element analyses, Fig. 4a compares the mean and standard deviation of the composition of N-MORB recovered within <1.5 km of the ridge axis, with the mean and standard deviation of the off-axis-type lavas. The signature of low-pressure olivine–plagioclase–clinopyroxene fractionation has been removed by correcting the compositions to a constant 7.3% MgO, which is the mean MgO content of the full data set[12,21]. Samples with MgO > 8.0% have been excluded because they may not lie on olivine–plagioclase–clinopyroxene fractionation trends. For clarity, all of the compositions are normalized by the mean of the axial N-MORB samples.

In terms of major elements, the OA-N-MORBs have signatures similar to the on-axis N-MORB, but tend to be less fractionated (higher MgO) on eruption, suggesting less cooling in the crust. The OA-N-MORBs are also characterized by unusually low abundances of trace elements that are incompatible during mantle melting (Ba to Sc) compared to N-MORB lavas from the ridge axis. This sense of off-axis depletion is the qualitative signature of models with convergent melt flow towards the ridge axis. This signal is clear in all incompatible trace elements with the possible exception of Sr which, while moderately incompatible during melting, behaves compatibly during low-pressure fractionation involving plagioclase. The variation in Sr content probably reflects more complex crustal fractionation processes than are accounted for by the corrections used here[11,12].

Although the differences in composition for the off-axis-type N-MORB are small (~20% less than the mean), they are also quantitatively consistent with the predictions of the models. Figures 4b and c compare the incompatible trace element data to the model calculations for passive flow, assuming a single bulk partition coefficient during melting and transport. These models are the same as those presented in ref. 9, and were calculated independently of the 12° N data. Nevertheless, the agreement between models and data is remarkably good, in both the overall shapes of the patterns

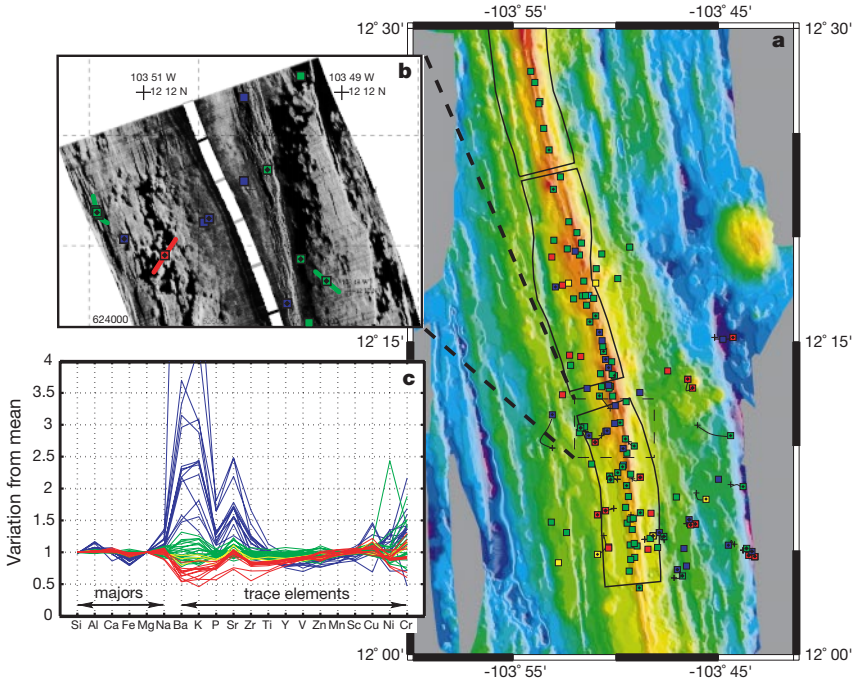

Figure 3 Map showing the location and composition of samples collected between 12° 00′ and 12° 30′ N on the East Pacific Rise[10–12]. **a**, Bathymetric relief map of the region, illuminated from the east[15]. Sea-floor depths increase away from the ridge axis, from red (~2,600 m) to purple (~3,200 m). The thin black lines outline SeaMARC I sonar images[16] that have been renavigated. Dredges are shown by short heavy lines with squares on top. Rock core locations are shown by isolated squares. Samples with filled diamonds have full major and trace-element analyses (**c**) and are used to classify the remaining partial samples. Blue squares indicate incompatible trace-element enriched T-MORB; green squares indicate N-MORB; red squares indicate the off-axis-type N-MORB. Yellow samples are intermediate between off-axis- and N-MORB. Details of sampling and analysis are given elsewhere[10–12]. **b**, Close-up map showing an example of sample locations superimposed on Sea-MARC I imagery. The short red dredge (VE10) is an off-axis-type lava and was collected from hummocky extrusive flows that cover older sea-floor faults. Highly reflective regions are bright (white), and shadows are black. The axial summit trough is the fissured region in the centre of the eastern strip. **c**, Compositional variation of samples with full major- and trace-element analyses corrected to 7.3% MgO. The colour scheme is the same as the sample map. Compositions are all normalized to the mean composition of the N-MORB samples.

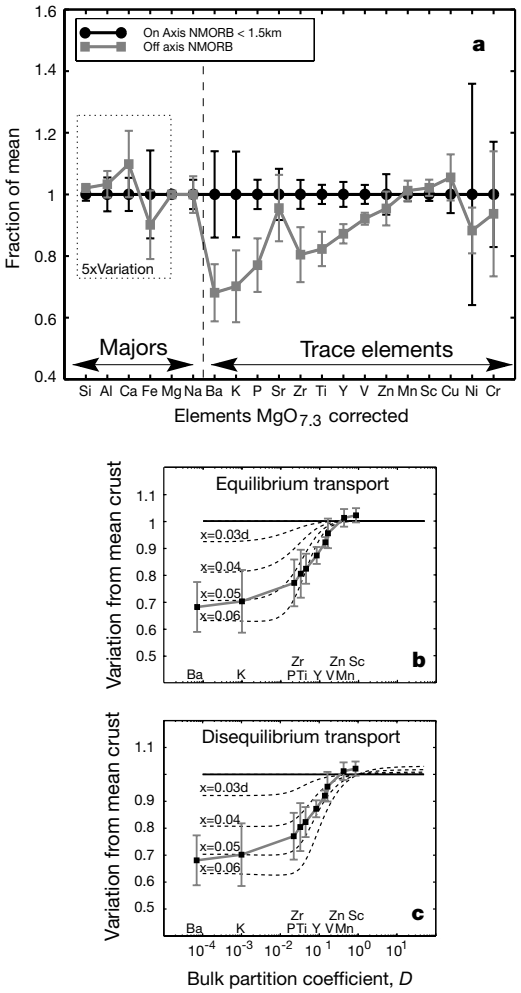

Figure 4 Comparison of on- and off-axis EPR magmas with model predictions. **a**, Major- and trace-element compositions of 12° N EPR basalt glasses with full analyses. Circles are the mean of 18 N-MORBs collected within <1.5 km of the axis, and the squares are the mean of 11 off-axis-type N-MORBs. The first six points are compositions of major-element oxides by microprobe, and the subsequent points are DCP analyses of trace elements shown roughly in order of compatibility. Variation from the mean in major elements for the first 5 elements is multiplied by a factor of 5. All values are fractionation-adjusted to 7.3% MgO and normalized to the mean of the on-axis N-MORB. Error bars show $\pm 1\sigma$ standard deviation which is a good proxy for the range of natural variation in each data group. **b**, Comparison of 12° N off-axis incompatible trace element patterns (squares) to model predictions for equilibrium melt transport in plate driven mantle flow with convergent melt migration (Fig. 1a). Compositions from the model are normalized to the model's mean ''crustal'' composition (thick lines in Fig. 2). Thin dashed lines indicate trace-element patterns calculated for various distances off-axis where the distance x is scaled to the depth of the melting region. The curve marked $x = 0.06d$ corresponds to the arrow in Fig. 1a, and would be 4.8 km for $d = 80$ km ($h = 6$ km). **c**, As **b** but for disequilibrium transport.

and the rough distances off-axis (of the order of several kilometres). Measured distances of samples, of course, should be used with caution in the absence of an independent estimate of the age of eruption. Analyses of U-series nuclides can provide information on eruption ages and crustal residence times up to ~300 kyr, and could provide an important independent test of these models in the future. Such measurements have already demonstrated clear off-axis eruptions at 9° 30′ N[17,19,22].

The quantitative comparison of data and models is expected to change as more data and additional processes are included in the models, but the qualitative result is robust. The important point is that the off-axis melts at 12° N appear more depleted in incompatible trace elements than the axial melts across a range of elements, consistent with convergent melt flow. Although there may be other mechanisms for convergent melt flow in addition to the model shown here (see, for example, refs 23, 24) these results probably rule out significant convergent solid flow within the partially molten region.

The results we report here are consistent with both geochemical and geophysical reasoning. Results from the seismic MELT experiment at 17° S on the southern EPR suggest that melt is distributed over a wide area at depth[8]. The simultaneous existence of a narrow neovolcanic zone at the surface implies some mechanism for lateral melt migration in the MELT area. Although seismic or electromagnetic techniques can sense the presence of melt, they probably cannot distinguish the relative geometries of melt and solid flow fields. However, our results suggest that geochemistry can make this distinction, because the geometry of melt and solid flow controls the mixing of melts and their interaction with different solid residues. We interpret the geochemical signatures at 12° N as the most direct evidence yet for lateral melt migration. □

Received 19 July; accepted 27 September 1999.

1. Spiegelman, M. & McKenzie, D. Simple 2-D models for melt extraction at mid-ocean ridges and island arcs. *Earth Planet. Sci. Lett.* **83,** 137–152 (1987).
2. Phipps Morgan, J. Melt migration beneath mid-ocean spreading centers. *Geophys. Res. Lett.* **14,** 1238–1241 (1987).
3. Scott, D. R. & Stevenson, D. J. A self-consistent model of melting, magma migration and buoyancy-driven circulation beneath mid-ocean ridges. *J. Geophys. Res.* **94,** 2973–2988 (1989).
4. Buck, W. R. & Su, W. Focused mantle upwelling below mid-ocean ridges due to feedback between viscosity and melting. *Geophys. Res. Lett.* **16,** 641–644 (1989).
5. Scott, D. R. in *Mantle Flow and Melt Generation at Mid-ocean Ridges* (eds Phipps Morgan, J., Blackman, D. K. & Sinton, J. M.) 327–352 (Geophysical Monogr. Vol. 71, American Geophysical Union, Washington DC, 1992).
6. Cordery, M. J. & Phipps Morgan, J. Convection and melting at mid-ocean ridges. *J. Geophys. Res.* **98,** 19477–19503 (1993).
7. Sparks, D. W. & Parmentier, E. M. The structure of three-dimensional convection beneath oceanic spreading centres. *Geophys. J. Int.* **112,** 81–91 (1993).
8. Forsyth, D. W. *et al.* Imaging the deep seismic structure beneath a mid-ocean ridge: the MELT experiment. *Science* **280,** 1215–1217 (1998).
9. Spiegelman, M. Geochemical consequences of melt transport in 2-D: The sensitivity of trace elements to mantle dynamics. *Earth Planet. Sci. Lett.* **139,** 115–132 (1996).
10. Reynolds, J. R., Langmuir, C. H., Bender, J. F., Kastens, K. A. & Ryan, W. B. F. Spatial and temporal variability in the geochemistry of basalts from the East Pacific Rise. *Nature* **359,** 493–499 (1992).
11. Reynolds, J. R. *Segment Scale Systematics of Mid-ocean Ridge Magmatism and Geochemistry.* (Thesis, Columbia Univ./LDEO, (1995).
12. Reynolds, J. R. & Langmuir, C. H. Identification and implications of off-axis lava flows around the East Pacific Rise. *Earth Planet. Sci. Lett.* (in the press).
13. Plank, T. & Langmuir, C. H. Effects of the melting regime on the composition of the oceanic crust. *J. Geophys. Res.* **97,** 19749–19770 (1992).
14. McKenzie, D. & O'Nions, R. K. Partial melt distributions from inversion of rare earth element concentrations. *J. Petrol.* **32,** 1021–1091 (1991).
15. Monti, S., Gente, P. & Maze, J. P. *Carte Batheymetrique de la Dorsale Est-Pacifique de 10° Nord a 14°30′ Nord* (IFREMER, Brest, 1987).
16. Crane, K. Structural evolution of the East Pacific Rise axis from 13° 10′N to 10° 35′N; interpretation from Sea-MARC I data. *Tectonophysics* **136,** 65–124 (1987).
17. Perfit, M. R. & Chadwick, W. W. Jr in *Faulting and Magmatism at Mid-Ocean Ridges* (eds Buck, R. W., Delaney, P. T., Karson, J. A. & Lagabrielle, Y.) 59–115 (Geophysical Monogr. Ser., Vol. 106, American Geophysical Union, Washington DC, 1998).
18. Detrick, R. S. *et al.* Multi-channel seismic imaging of a crustal magma chamber along the East Pacific Rise. *Nature* **326,** 35–41 (1987).
19. Perfit, M. R. *et al.* Small-scale spatial and temporal variations in midocean ridge crest magmatic processes. *Geology* **22,** 375–397 (1994).
20. Perfit, M. R. *et al.* Detailed petrological and geochemical studies of on- and off-axis lavas from the East Pacific Rise; 9°30′–10°N. *Eos* **75,** 601 (1994).
21. Weaver, J. S. & Langmuir, C. H. Calculation of phase equilibrium in mineral-melt systems. *Comput. Geosci.* **16,** 1–19 (1990).
22. Goldstein, S. J., Perfit, M. R., Batiza, R., Fornari, D. J. & Murell, M. T. Off-axis volcanism at the East Pacific Rise detected by uranium-series dating of basalts. *Nature* **367,** 157–159 (1994).
23. Sparks, D. W. & Parmentier, E. M. Melt extraction from the mantle beneath spreading centers. *Earth Planet. Sci. Lett.* **105,** 368–377 (1991).
24. Spiegelman, M. Physics of melt extraction: Theory, implications and applications. *Phil. Trans. R. Soc. Lond. A* **342,** 23–41 (1993).

Acknowledgements

We thank M. Perfit for comments and suggestions, and C. H. Langmuir and P. Asimow for discussions. This work was supported by NSF-OCE.

Correspondence and requests for materials should be addressed to M.S. (e-mail: mspieg@ldeo.columbia.edu).